Nonadiabatic quantum fluctuations in the neutral ground state of tetrathiafulvalene-*p*-chloranil

Yuko Watanabe,[1] Hideo Ando,[1] Akira Takahashi,[2] and Norikazu Tomita[1]

[1]*Department of Physics, Faculty of Science, Yamagata University, 1-4-12 Kojirakawa-machi, Yamagata, Yamagata 990-8560, Japan*
[2]*Graduate School of Engineering, Nagoya Institute of Technology, Gokiso-cho, Showa-ku, Nagoya, Aichi 466-8555, Japan*

(Received 9 August 2019; revised manuscript received 1 November 2019; published 27 November 2019)

A nonadiabatic resonating Hartree-Fock method is applied to the one-dimensional extended Hubbard model with a staggered site-diagonal potential and Su-Schrieffer-Heeger-type electron-phonon coupling to clarify the lattice and electronic structures in the charge-density-wave (CDW) ground state. It is shown that small spin-Peierls-type domains and large dimerized CDW domains appear in the main CDW state having an equidistant lattice. Interference of breathing and translational motions of these domains constitutes quantum fluctuations. The natures of different domains are analyzed by Löwdin-Feshbach partitioning method. The present results, indicating the domains in the CDW ground state as quantum fluctuations, are consistent with the experimentally observed THz electric-field-induced changes in the electronic dipole moment in the neutral phase of tetrathiafulvalene-*p*-chloranil (TTF-CA).

DOI: 10.1103/PhysRevB.100.205205

I. INTRODUCTION

Over the last century, a large body of research has investigated organic charge transfer (CT) complexes, which exhibit a lot of exotic phenomena, such as superconductivity and photoinduced phase transition, due to the strong electron-phonon and electron-electron interactions. The soft lattice structures of organic CT complexes can easily change by temperature or photoirradiation. With these structural changes, they exhibit a rich variety of ground and excited states, such as charge ordered, spin-Peierls, and superconducting states, some of which are caused by the strong electron-electron interaction. Thus, organic CT complexes are archetypal target materials to experimentally investigate the many-body effects with an eye to fundamental understanding and also practical use.

In theory, on the other hand, it is still challenging to simultaneously describe the electron-phonon and electron-electron interactions. The many-variable variational Monte Carlo (mVMC) method is a promising approach to incorporate all kinds of many-body effects in all dimensions [1]. The density matrix renormalization group (DMRG) method is also a powerful approach for one-dimensional systems [2,3]. To gain further intuitive understanding of the many-body effects including the nonadiabatic ones in the quantized lattice, we have recently extended a resonating Hartree-Fock (ResHF) method to electron-phonon coupled systems. In this method, direct products of the Slater determinants and the coherent state representations of phonons are superposed. All the orbitals in the Slater determinants and probability amplitudes in the coherent states are optimized. By visualizing the electronic and lattice structures of the optimized Slater determinants and coherent states, the nonadiabatic ResHF method provides intuitive understanding of the quantum fluctuations. In a previous paper, we have applied the method to the one-dimensional extended Hubbard model with Su-Schrieffer-Heeger (SSH)-type electron-phonon coupling [4] and clarified the mechanism of the insulator-metal transition in doped transpolyacetylene [5,6].

In the present paper, we apply the method to the one-dimensional extended Hubbard model with a staggered site-diagonal potential [7–13] and SSH-type electron-phonon coupling [14–17]. We focus on the electron and lattice structures of the charge-density-wave (CDW) ground state. This model is often used to investigate the electron and lattice structures of tetrathiafulvalene-*p*-chloranil (TTF-CA). At $T = 81$ K, TTF-CA exhibits a neutral-ionic phase transition, where the amount of charge transfer from TTF molecules to CA molecules significantly changes from 0.3 (neutral phase) to 0.6 (ionic phase) [18–20]. Small charge transfer in the neutral phase means large (small) electron density at TTF (CA) molecule, and the state corresponds to the CDW state. On the other hand, large charge transfer in the ionic phase means nearly equal electron density at TTF and CA molecules. Interestingly, this electronic change accompanies a structural change of the lattice. The neutral phase has an equidistant lattice, while the ionic phase has a dimerized lattice. As a localized spin lies at each molecule, this ionic phase can be regarded as a spin-Peierls state. This is attributed to the strong Coulomb interaction in TTF-CA. Thus, TTF-CA is a good target material to investigate the many-body effects due to both the electron-electron interaction and electron-phonon coupling. TTF-CA is also famous for its electronic-type ferroelectricity in the ionic phase. In contrast to the conventional ferroelectricity (e.g., displacive-type ferroelectricity), the charge transfer from TTF molecules to CA molecules itself is the origin of the electronic-type ferroelectricity [21]. Recently, it was shown that this ferroelectricity can be controlled in a subpicosecond time scale by THz electric fields [22]. This success proved that TTF-CA is a promising candidate material for ultrafast electric devices. Morimoto *et al.* applied a similar

THz pulse to the neutral phase. Although this phase does not show the ferroelectricity, they have succeeded in showing that a large macroscopic polarization was generated by the THz electric field [23]. They concluded that there are two different contributions to the electric-field-induced polarization. One is a fast-following intermolecular charge transfer and the other is a slower breathing motion of domain walls connecting the neutral state and the ionic state. In addition, the observed reflectivity change indicated a coherent oscillation related to the lattice dimerization in the ionic domains. This is because the spin-Peierls dimerization is necessary to realize the ionic state. All these demonstrate the robustness of the electron-electron and electron-phonon interactions in TTF-CA and the critical importance of theoretical calculations of the electron and lattice structures beyond the adiabatic approximation.

We will show that small spin-Peierls domains appear in the CDW state in the ResHF wave function. Rather wide dimerized CDW regions (dimerized domains) also appear in the main CDW state with an equidistant lattice. The quantum fluctuations in the CDW state can be explained by the breathing and translational motions of these two kinds of domains. Although our theory cannot describe the dynamics of the electron or lattice, the present results strongly suggest that spin-Peierls domains really exist and the almost instantaneous polarization response to the THz electric field would be attributed to these spin-Peierls domains and dimerized domains, inherent in the ground-state wave function as quantum fluctuations. In the past, many researchers thought that the CDW phase was fully understood. The CDW phase of TTF-CA was a somewhat uninteresting state without ferroelectricity. Nevertheless, the recent THz pump-probe study [23] has demonstrated the possibility that the structures and the motions of small local domains in the uniform CDW phase, whose spatial/temporal monitoring is extremely difficult, can play a critical role in the macroscopic polarization of TTF-CA. The CDW state has come back as a challenging and fascinating topic. By shedding light on the quantum fluctuations inherent but obscured in the regular CDW phase, our study clarifies how electronic structures and lattice structures are mutually coupled beyond the adiabatic (classical) pictures and thereby provides new suggestions that will serve a basis for interpreting and controlling the ultrafast polarization of the CDW state of TTF-CA. By using the Löwdin-Feshbach partitioning method [24–29], we also investigate how spin-Peierls domain states are stabilized and mutually superposed under the influence of dimerized domain states. The present paper provides a clear picture of quantum fluctuations in the electron and (quantized) lattice structures of TTF-CA beyond the adiabatic approximation.

The paper is organized as follows. In Sec. II and III, we briefly review our model and method. In Sec. IV A, we analyze the ResHF wave functions in terms of domain structures and their system-size dependence. In Sec. IV B, the nature of the quantum fluctuation is further discussed by using Löwdin-Feshbach partitioning method. In Sec. IV C, we provide a theoretical insight into the subpicosecond dynamics of TTF-CA initiated by a pump pulse. Finally, we give a brief summary in Sec. V.

II. MODEL

We use the following model Hamiltonian for the one-dimensional chain of TTF-CA:

$$\begin{aligned} H = &-\sum_{l=1}^{N}\sum_{\sigma=\uparrow,\downarrow}[t-\alpha(q_{l+1}-q_l)](c^{\dagger}_{l+1,\sigma}c_{l,\sigma}+c^{\dagger}_{l,\sigma}c_{l+1,\sigma}) \\ &+\Delta\sum_{l=1}^{N}(-1)^l n_l+\sum_{l=1}^{N}\left[\frac{p_l^2}{2M}+\frac{K}{2}(q_{l+1}-q_l)^2\right] \\ &+U\sum_{l=1}^{N}n_{l,\uparrow}n_{l,\downarrow}+V\sum_{l=1}^{N}n_{l+1}n_l, \end{aligned} \tag{1}$$

where N is the system size. $c^{\dagger}_{l,\sigma}$ ($c_{l,\sigma}$) is a creation (annihilation) operator of an electron with spin σ at the lth site, and the relevant number operator is given by $n_{l,\sigma}=c^{\dagger}_{l,\sigma}c_{l,\sigma}$. The first term of Eq. (1) represents the transfer of electrons with SSH electron-phonon coupling [4]. The parameters t and α denote the transfer energy for the uniform equidistant lattice and the electron-phonon coupling constant, respectively. The operator q_l denotes the lattice displacement from the equidistant position at the lth site, which is scaled by the lattice constant of TTF-CA in the CDW ground state with the equidistant lattice. Due to this scaling, α has the dimension of energy. See Supplemental Material [30] for further details regarding the scaling. $\alpha(q_{l+1}-q_l)$ is the linear deviation of the transfer energy from t for the equidistant lattice. This linear deviation approximation of the transfer energy is valid when the lattice displacement is small. In the case of TTF-CA, the neutron diffraction experiment showed that the CDW state has an equidistant lattice [19]. Even in the spin-Peierls ground state, the lattice distortion is only a few percent of the lattice constant [19]. Therefore, the linear deviation approximation works well for TTF-CA. n_l in the second term is the total number operator of electron at the lth site, that is, $n_l=n_{l,\uparrow}+n_{l,\downarrow}$. The site with odd l has the highest occupied molecular orbital (HOMO) of the neutral TTF molecule, while the site with even l has the lowest unoccupied molecular orbital (LUMO) of the neutral CA molecule. 2Δ denotes the energy difference between these molecular orbitals. The third term represents the lattice Hamiltonian $H_{\rm ph}$, where we approximately use the equal mass M for both the TTF and CA lattice points. p_l denotes the momentum of the lth lattice point and K is the lattice elastic constant. We assume the harmonic oscillation of the lattice. In TTF-CA, as mentioned above, the lattice deviation from the equidistant lattice is very small and, therefore, nonharmonic effects can be negligible. In our Hamiltonian, since the lattice deviation is scaled by the lattice constant, K has the dimension of energy. U in the fourth term and V in the last term denote the on-site and the nearest-neighbor-site Coulomb interaction, respectively. We impose a periodic boundary condition on this model and thus

$$c^{\dagger}_{N+1,\sigma}=c^{\dagger}_{1,\sigma},\quad q_{N+1,\sigma}=q_{1,\sigma},\quad p_{N+1,\sigma}=p_{1,\sigma}. \tag{2}$$

In this study, we treat not only electrons but also lattice quantum mechanically. Using Fourier transformation,

$$q_l = \frac{1}{\sqrt{N}} \sum_{-\pi<k\leqslant\pi} Q_k e^{ikl}, \quad p_l = \frac{1}{\sqrt{N}} \sum_{-\pi<k\leqslant\pi} P_k e^{-ikl}, \quad (3)$$

the lattice Hamiltonian can be rewritten as

$$H_{\rm ph} = \frac{1}{2M} \sum_{-\pi<k\leqslant\pi} P_k P_k^\dagger + \frac{M}{2} \sum_{-\pi<k\leqslant\pi} \omega_k^2 Q_k^\dagger Q_k, \quad (4)$$

where

$$\omega_k = \omega \left|\sin\frac{k}{2}\right|, \quad \omega = 2\sqrt{\frac{K}{M}}. \quad (5)$$

In addition, we define the creation and annihilation operators of a phonon with mode k as

$$b_k^\dagger = \frac{M\omega_k Q_k^\dagger - iP_k}{\sqrt{2M\hbar\omega_k}}, \quad b_k = \frac{M\omega_k Q_k + iP_k^\dagger}{\sqrt{2M\hbar\omega_k}}. \quad (6)$$

Thus, we get the following quantized lattice Hamiltonian

$$H_{\rm ph} = \sum_{-\pi<k\leqslant\pi} \hbar\omega_k \left(b_k^\dagger b_k + \frac{1}{2}\right), \quad (7)$$

where $\hbar$ is the reduced Planck constant. From Eqs. (3) and (6), q_l and p_l are given by

$$q_l = \sum_{-\pi<k\leqslant\pi} \sqrt{\frac{\hbar}{2MN\omega_k}} (b_k + b_{-k}^\dagger) e^{ikl}, \quad (8)$$

$$p_l = \sum_{-\pi<k\leqslant\pi} i\sqrt{\frac{M\hbar\omega_k}{2N}} (b_k^\dagger - b_{-k}) e^{-ikl}. \quad (9)$$

We thereby treat $\{q_l\}$ and $\{p_l\}$ quantum mechanically.

To describe the CDW ground state of TTF-CA, we use the following parameters:

$$t = 1, \quad U = 10, \quad V = 4.5, \quad \Delta = 0.65, \quad \text{and}$$
$$\hbar\omega = 0.07. \quad (10)$$

In practical calculations, we set $\hbar = 1$. The electron-phonon coupling constant α and the lattice elastic constant K are set at

$$\alpha = 0.35, \quad K = 0.4, \quad (11)$$

which are determined to approximately realize the lattice structures of the neutral and ionic phases of TTF-CA. The system has an equidistant lattice in the neutral phase while it has a dimerized lattice in the ionic phase. In the previous paper [31], they used the parameters, as

$$\lambda = \frac{\alpha^2}{tK} = 0.55, \quad (12)$$

where λ is a dimensionless electron-phonon coupling constant [32]. On the other hand, our parameters give $\lambda = 0.31$. Although our λ is smaller than the previous one, the difference does not affect the qualitative features we will describe below. This would be because our parameter regime of U, V, and Δ is rather far from the phase boundary. When using these parameters for Eq. (1), the CDW state becomes the ground state of this system. In this paper, the energy is scaled by transfer energy t. For TTF-CA, t is estimated as $t = 0.17$ eV by a band calculation [33]. This value of the transfer energy is also consistent with the previously employed one in Ref. [34]. U and V are determined to approximately reproduce the optical gap energy around 0.5 eV with $t = 0.17$ eV [13]. ω is roughly estimated by using the Raman spectrum in Ref. [22].

III. METHOD

Here, we briefly review a ResHF method for a many-fermion system. First, we prepare a basis set $\boldsymbol{\chi} = \{\chi_i\}, i = 1, \ldots, N$. In the present case, χ_i is the HOMO of TTF when i is odd. On the other hand χ_i is the LUMO of CA when i is even. We construct the occupied molecular orbitals for spin σ of the fth Slater determinant $\boldsymbol{\varphi}_{f,\sigma} = [(\boldsymbol{\varphi}_{f,\sigma})_\alpha]$ by a linear combination of the basis set, such as

$$(\boldsymbol{\varphi}_{f,\sigma})_\alpha = \sum_{i=1}^{N} (\boldsymbol{U}_{f,\sigma})_{i,\alpha} \chi_i, \quad (13)$$

where $\boldsymbol{U}_{f,\sigma} = [(\boldsymbol{U}_{f,\sigma})_{i,\alpha}]$ is the $N \times N_\sigma$ matrix satisfying $\boldsymbol{U}_{f,\sigma}^\dagger \boldsymbol{U}_{f,\sigma} = \boldsymbol{I}$. Here, N_σ is the number of electrons with spin σ. It should be noted that we employ the different orbitals for different spins (DODS). Then, if we define $c_{i,\sigma}^\dagger$ as a creation operator applying to the $\boldsymbol{\chi}$ space, a creation operator $f_{\alpha,\sigma}^\dagger$ applying to the $\boldsymbol{\varphi}_{f,\sigma}$ space is given by

$$f_{\alpha,\sigma}^\dagger = \sum_{i=1}^{N} (\boldsymbol{U}_{f,\sigma})_{i,\alpha} c_{i,\sigma}^\dagger. \quad (14)$$

Thus, we can define the fth Slater determinant by

$$|\psi_f\rangle = \prod_{\sigma=\uparrow,\downarrow} \prod_{\alpha}^{occ} f_{\alpha,\sigma}^\dagger |0^{(e)}\rangle, \quad (15)$$

where $|0^{(e)}\rangle$ is the vacuum of electrons. In the ResHF method, we generate a many-body wave function by the superposition of such Slater determinants,

$$|\Psi\rangle = \sum_{f=1}^{N_S} C_f \sum_{G}^{N_G} P^G |\psi_f\rangle. \quad (16)$$

We usually use the symmetry-broken DODS-type orbitals for the Slater determinants. P^G in Eq. (16) schematically represents symmetry projections to preserve the original symmetry of the system, and N_G is the number of these projections. In practical calculations, we carry out the Peierls-Yoccoz projections [35] to recover the spatial symmetry of the system represented by $D_{N/2}$. We also apply the half projection [36,37] to the wave function to approximately obtain the spin-singlet state. The total number of the superposition is $N_S \times N/2$ (to recover the $C_{N/2}$ translation symmetry) $\times 2$ (to recover the spatial inversion symmetry at the site center) $\times 2$ (spin half projection to remove the triplet component). We variationally determine all the unitary matrices $\boldsymbol{U}_{f,\sigma}$ (orbital optimization) as well as the superposition coefficients. The details of the optimization procedures are given in Ref. [38]. The Slater determinants generating the ResHF wave function

TABLE I. Comparison of the energies E and correlation energies E_{CORR} obtained with the HF, ResHF, and ED methods ($U = 10, V = 4.5, \Delta = 0.65, N = 14$).

Method	E	E_{CORR}	(%)
HF	55.580	0	0
ResHF($N_S = 3$)	55.217	0.363	93
ResHF($N_S = 15$)	55.195	0.385	99
ED	55.191	0.389	100

are nonorthogonal to each other, as

$$\langle\psi_f|\psi_g\rangle = \prod_{\sigma=\uparrow,\downarrow} \det(\boldsymbol{U}^{\dagger}_{f,\sigma}\boldsymbol{U}_{g,\sigma}) \neq 0. \tag{17}$$

If the electron correlation is small, the perturbation or the low order configuration interaction from the Hartree-Fock (HF) state is accurate enough to describe the system. However, if the electron correlation is significantly large, the interaction modifies the orbital structures deeply below the highest occupied orbital. We call such a large correlation effect, which cannot be described by the perturbation or low order configuration interaction, a static correlation effect. As the ResHF wave function has independent nonorthogonal molecular orbital sets for different Slater determinants, it can efficiently describe the static correlation effects, compared to the orthogonal multiconfiguration approach which has only a single molecular orbital set, just exchanging the occupied and unoccupied orbitals. This is the main reason why the ResHF wave function can describe the electron correlation effects efficiently [39,40].

Furthermore, we give physics to the quantum fluctuations in terms of quantum interference of the relevant states. For this purpose, we first investigate the HF ground and excited states and guess what states would be relevant to the correlated ground state. This is a standard guideline for choosing trial Slater determinants generating the ResHF wave function. Then we optimize all the orbitals of the Slater determinants. The orbital optimization is important to obtain the accurate wave function. Even if we choose wrong trial Slater determinants, the orbital optimization modifies the orbitals to yield the accurate wave function. To check the accuracy of the ResHF wave function, we carried out the exact diagonalization (ED) calculation for the present model ($U = 10, V = 4.5, \Delta = 0.65$ at $N = 14$). For simplicity, we employed the adiabatically fixed equidistant lattice in this benchmark calculation. The ground state energy E and the correlation energy E_{CORR} of every method are shown in Table I. We note that E_{CORR} is defined by

$$E_{\mathrm{CORR}} = E_{\mathrm{HF}} - E, \tag{18}$$

where E_{HF} represents the HF energy. As can be seen in Table I, the exact ground state energy is 55.191 in units of t, while the unrestricted HF energy is 55.580. The ResHF energy is 55.217 in the case of $N_S = 3$, and it becomes 55.195 in the case of $N_S = 15$. Thus, 93% of the exact correlation energy is explained by the superposition of only three Slater determinants. 99% of the correlation energy is explained with 15 Slater determinants. We can thus safely say that the ResHF method works well for the present model.

Recently, we extended the ResHF method to electron-phonon coupled systems. To describe the lattice, we employ the coherent state representation of phonons, such as

$$|\phi_f\rangle = e^{-|\boldsymbol{z}_f|^2/2} e^{\boldsymbol{z}_f\cdot\boldsymbol{b}^{\dagger}}|0^{(ph)}\rangle, \tag{19}$$

where

$$\boldsymbol{z}_f = (z_{f,1}, z_{f,2}, \ldots, z_{f,N}), \quad \boldsymbol{b}^{\dagger} = (b_1^{\dagger}, b_2^{\dagger}, \ldots, b_N^{\dagger}). \tag{20}$$

Here, $|0^{(ph)}\rangle$ is the vacuum of phonons and $z_{f,k}$ is the probability amplitude of the phonon with mode k in the fth lattice state. The coherent state has nonorthogonality:

$$\langle\phi_f|\phi_g\rangle = \exp\left[\boldsymbol{z}_f^*\cdot\boldsymbol{z}_g - \frac{|\boldsymbol{z}_f|^2 + |\boldsymbol{z}_g|^2}{2}\right] \neq 0. \tag{21}$$

The coherent state $|\phi_f\rangle$ is an eigenstate of the annihilation operator b_k and the corresponding eigenvalue is $z_{f,k}$:

$$b_k|\phi_f\rangle = z_{f,k}|\phi_f\rangle. \tag{22}$$

Using Eqs. (8), (9), and (22), we obtain the following equations:

$$\langle\phi_f|q_l|\phi_f\rangle = \sum_{-\pi<k\leqslant\pi} \sqrt{\frac{\hbar}{2MN\omega_k}}(z_{f,k} + z^*_{f,-k})e^{ikl}, \tag{23}$$

$$\langle\phi_f|p_l|\phi_f\rangle = \sum_{-\pi<k\leqslant\pi} i\sqrt{\frac{M\hbar\omega_k}{2N}}(z^*_{f,k} - z_{f,-k})e^{-ikl}. \tag{24}$$

Since we consider the solid state, the expectation value $\langle\phi_f|p_l|\phi_f\rangle$ in Eq. (24) should be zero. Then, we obtain

$$z^*_{f,-k} = z_{f,k}. \tag{25}$$

Using Eq. (25), Eq. (23) can be rewritten as

$$\langle\phi_f|q_l|\phi_f\rangle = \sum_{-\pi<k\leqslant\pi} \sqrt{\frac{2\hbar}{MN\omega_k}} z_{f,k}e^{ikl}. \tag{26}$$

We can determine the lattice structure from $\{z_{f,k}\}$.

The nonadiabatic ResHF wave function is constructed by the superposition of direct products of nonorthogonal Slater determinants $|\psi_f\rangle$ for electrons and coherent states $|\phi_f\rangle$ for phonons:

$$\begin{aligned}|\Psi\rangle &= \sum_{f=1}^{N_S} C_f\left[\sum_{G}^{N_G} P^G(|\psi_f\rangle\otimes|\phi_f\rangle)\right]\\ &= \sum_{f=1}^{N_S} C_f \sum_{G}^{N_G} P^G|\psi_f,\phi_f\rangle,\end{aligned} \tag{27}$$

where C_f's are the superposition coefficients and N_S is the number of the nonorthogonal bases $\{|\psi_f,\phi_f\rangle\}$. By superposing the coherent states, we can efficiently describe large quantum fluctuations beyond the adiabatic approximation, such as the breathing motions of topological lattice defects.

In the present ResHF wave function, $\{C_f|f = 1,\ldots,N_S\}$, $\{\boldsymbol{U}_{f,\sigma}|f = 1,\ldots,N_S,\ \sigma =\uparrow,\downarrow\}$, and $\{\boldsymbol{z}_f|f = 1,\ldots,N_S\}$ are variationally determined [5,38,41]. In other words, electronic

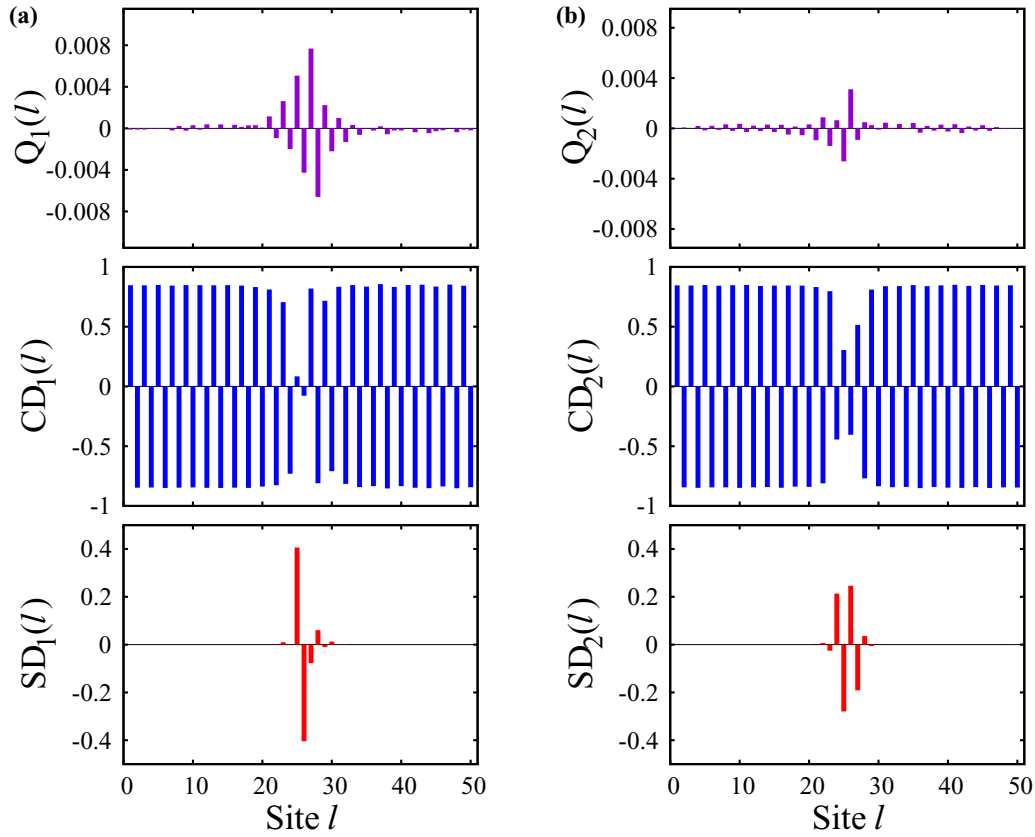

FIG. 1. Structures of two Slater determinants and coherent states, (a) $|\psi_1, \phi_1\rangle$ and (b) $|\psi_2, \phi_2\rangle$, for $(N, N_S) = (50, 7)$. The weight of each state is the following: $W_1 = 0.1914$ and $W_2 = 0.1658$.

states and lattice structures are determined to minimize the energy:

$$E = \frac{\langle\Psi|H|\Psi\rangle}{\langle\Psi|\Psi\rangle}. \tag{28}$$

In the present model, we found that the spin-Peierls-type domains in the CDW state are relevant in the HF approximation (though we omit these HF results). To describe the quantum breathing motion of such spin-Peierls domains (quantum interference among domains of different sizes), we superposed the Slater determinants having the spin-Peierls domains of different sizes, as a trial wave function. Then, we optimized all the orbitals of the Slater determinants generating the ResHF wave function. We also employed different trial wave functions, having topological solitons, lattice solitons, etc. However, after the orbital optimization, these solitons disappeared and the spin-Peierls domains appeared in the CDW states. In addition, even though we started with the equidistant lattice, the dimerized CDW domains appeared in the substantial equidistant CDW state, as shown below, after the lattice optimization.

IV. RESULTS AND DISCUSSION

A. Nonadiabatic ResHF solutions and quantum fluctuations

We apply the nonadiabatic ResHF method to the model given by Eq. (1) in order to reveal the quantum fluctuations of electron and lattice in the CDW ground state. We calculate the ResHF wave function for $N = 50$ and $N = 122$ to examine the system-size dependence. Before showing our results, we define the following physical quantities for analyzing the Slater determinants and coherent states:

$$Q_f(l) = \langle\psi_f, \phi_f|q_l|\psi_f, \phi_f\rangle, \tag{29}$$

$$CD_f(l) = \langle\psi_f, \phi_f|(n_l - 1)|\psi_f, \phi_f\rangle, \tag{30}$$

$$SD_f(l) = \frac{1}{2}\langle\psi_f, \phi_f|(n_{l,\uparrow} - n_{l,\downarrow})|\psi_f, \phi_f\rangle, \tag{31}$$

$$W_f = \frac{\left|\sum_G^{N_G}\langle\Psi|P^G|\psi_f, \phi_f\rangle\right|^2}{\sum_{f=1}^{N_S}\left|\sum_G^{N_G}\langle\Psi|P^G|\psi_f, \phi_f\rangle\right|^2}. \tag{32}$$

$Q_f(l)$ is the lattice displacement from the equidistant position of the lth site in the fth electron-lattice state $|\psi_f, \phi_f\rangle$. A positive (negative) value of $Q_f(l)$ indicates that the lth lattice point moves to the right (left). $CD_f(l)$ and $SD_f(l)$ represent the charge density minus 1 and the spin density at the lth site in $|\psi_f, \phi_f\rangle$, respectively. In addition, W_f denotes the weight of $|\psi_f, \phi_f\rangle$ in the wave function $|\Psi\rangle$. We should note that the denominator in Eq. (32) is not equal to 1 because of the nonorthogonality.

First, we show the structures of the ResHF wave function for $N = 50$ with $N_S = 7$ configurations. To save the space, the structures of two configurations are shown in Fig. 1. The configuration shown in Fig. 1(a) has the largest weight, while the one in Fig. 1(b) has the widest domain, whose characteris-

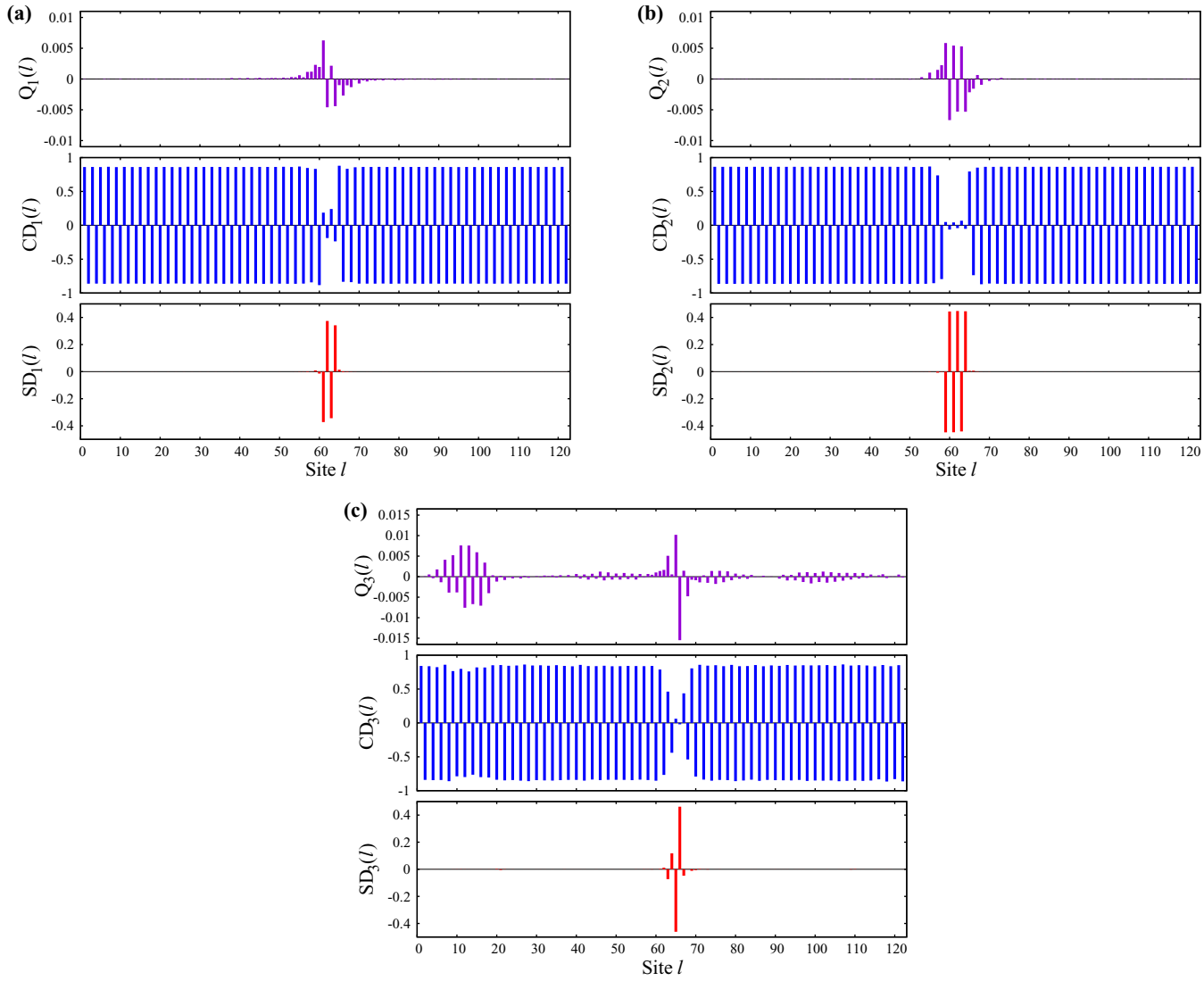

FIG. 2. Structures of three Slater determinants and coherent states, (a) $|\psi_1, \phi_1\rangle$, (b) $|\psi_2, \phi_2\rangle$, and (c) $|\psi_3, \phi_3\rangle$, for $(N, N_S) = (122, 35)$. The weight of each state is the following: $W_1 = 0.0664$, $W_2 = 0.0629$, and $W_3 = 0.0188$.

tics will be explained below. Although the symmetry of these configurations is broken, the symmetry of the wave function $|\Psi\rangle$ is restored by projection P^G in Eq. (27). From the middle and bottom panels of Fig. 1(a), we can see that the CDW structure is suppressed and the spin-density-wave (SDW) structure arises around the 25th and 26th sites. In addition, from the top panel of Fig. 1(a), we can see that this domain shows the lattice dimerization. Thus, we can regard this defect as a spin-Peierls domain. In TTF-CA, the CDW state corresponds to the neutral state with nearly doubly occupied HOMOs of TTF and empty LUMOs of CA, and the spin-Peierls domain corresponds to the ionic domain generated by HOMO-LUMO charge transfer in the neutral phase. The configuration shown in Fig. 1(b) has a slightly wider spin-Peierls domain around the 24th to 27th sites. The other configurations have similar structures, though the size of the spin-Peierls domain or the amplitude of the lattice distortion is slightly different. Thus, the ResHF wave function clearly shows that the spin-Peierls domain inherently exists as a quantum fluctuation in the CDW ground state. Furthermore, the superposition of these spin-Peierls domains of different sizes, as in Fig. 1(a) and 1(b), represents the quantum breathing motion of the spin-Peierls domain. In addition, the Peierls-Yoccoz projections to recover the translation symmetry represent the quantum translational motions of the spin-Peierls domains. Thus, the quantum fluctuations in the CDW phase are physically described by translation and breathing motions of the spin-Peierls domains.

Next, we show the structures of the wave function for $N = 122$ with $N_S = 35$ configurations. Figure 2 shows the structures of three configurations. The one in Fig. 2(a) has the largest weight, and the one in Fig. 2(b) has the widest spin-Peierls domain among 35 configurations. These two configurations have only spin-Peierls domains, while the one in Fig. 2(c) also has wide dimerized domains explained below. The other configurations, which are not shown here, have similar structures. As in the case of the wave function for $N = 50$, all configurations have spin-Peierls domains. From Fig. 2(c), we can also see that the dimerization appears even in the CDW region around the 5th to 20th and the 95th to 110th

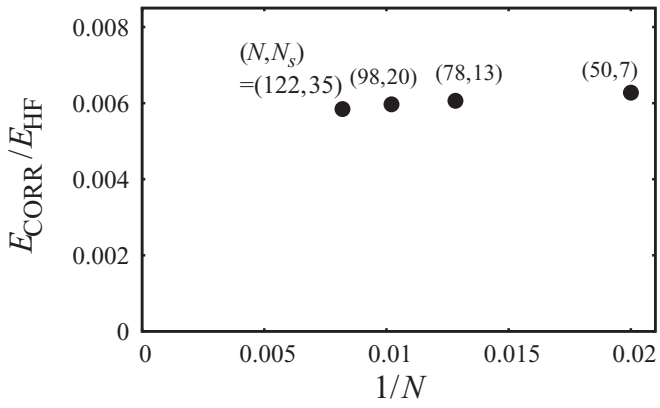

FIG. 3. System-size dependence of $E_{\mathrm{CORR}}/E_{\mathrm{HF}}$.

sites. Hereafter, we call these dimerized CDW regions dimerized domains. Although such dimerized domains are relatively large, the spin-Peierls domain stays small even in $N = 122$. This would be because the energy of the spin-Peierls state is significantly higher than the CDW state in the present parameter regime. As a result, the superposition of wider spin-Peierls domains cannot lower the ground state energy, and wide spin-Peierls domains cannot exist even as a quantum fluctuation. Thus, the present result strongly suggests that the density of the spin-Peierls domain should become zero in the thermodynamic limit. Now a question arises how and whether such quantum fluctuations of zero-density spin-Peierls domains can play a decisive role in the thermodynamic limit, especially in gaining the finite correlation energy. In the ResHF wave function, we apply the symmetry projection to all the configurations. In the thermodynamic limit, Peierls-Yoccoz projection for each configuration to recover the translation symmetry corresponds to the superposition of the infinite number of (two sites, four sites,..., N sites) translated configurations. The superposition of such an infinite number of symmetry adapted configurations, each of which contains the finite-size (zero-density) spin-Peierls domain, would gain the finite correlation energy in the thermodynamic limit. To validate this idea, we show in Fig. 3 the system-size dependence of the ratio of energy difference between the ResHF and HF states to the HF energy. As can be seen from Fig. 3, the ratio $E_{\mathrm{CORR}}/E_{\mathrm{HF}}$ is nearly constant and likely to converge to a finite value in the thermodynamic limit. Thus, we can say that the quantum fluctuations due to the finite-size (zero-density) spin-Peierls domains can work to stabilize the CDW ground state in the thermodynamic limit. On the other hand, the size of a dimerized domain is rather large and its density (the ratio of the size of the dimerized domain to the system) seems finite in the thermodynamic limit. Translation and breathing motions of such dimerized domains also make quantum fluctuations in the CDW ground state. We will see the role of the dimerized domain in the next subsection.

B. Nonorthogonal configuration interaction calculations and Löwdin-Feshbach partitioning analysis

To further study the natures and the origins of quantum fluctuations in the ResHF wave functions, we skipped the orbital and coherent-state optimizations described in Sec. III, thereby performing nonorthogonal configuration interaction (NOCI) calculations. To analyze the characteristics of the spin-Peierls domains and the dimerized domains found above, it is worth, to begin with, separately examining two different Hilbert spaces. P space is spanned by $\{|\Phi_i^P\rangle\}$, where $|\Phi_1^P\rangle$ is the CDW ground state in the HF theory and the rest of the bases $[i = 2, 3, \ldots, dim(P)]$ have a spin-Peierls domain across $2(i-1)$ sites. Hereafter the energy of $|\Phi_1^P\rangle$ will be denoted by E_{CDW}. Q space is spanned by $\{|\Phi_i^Q\rangle\}$, each of which has a dimerized domain across $2i$ sites $[i = 1, 2, \ldots, dim(Q)]$. The NOCI bases in P or Q space are constructed by referring to the charge density, spin density, and lattice displacement in the spin-Peierls or the dimerized domains of the ResHF solutions. To extract simple physical pictures, spin-Peierls or dimerized domains with homogeneous density/lattice structures are inserted in the regular CDW phase, which makes sharp domain boundaries. As compared to the ResHF wave functions (Figs. 1 and 2), the density/lattice structures of our NOCI bases sharply change across a domain boundary (see Fig. 4 for the spin-Peierls and the dimerized domain whose widths are eight sites). Every NOCI basis, like in the ResHF wave function in Eq. (27), is a symmetry-adapted projection of the product of a Slater determinant and a coherent state. Even though the expansion lengths employed are short, i.e., $dim(P) = 25$ and $dim(Q) = 24$, and no orbital and coherent-state optimizations are performed, the NOCI method in $P + Q$ space accounts for 37% of the correlation energy of the ResHF method for $N = 122$. This suggests that the NOCI solutions are useful for qualitative understanding of the ResHF wave functions.

We obtained the P-space NOCI eigenstates [$N = 122$ and $dim(P) = 25$], whose spin-Peierls domain widths were analyzed in terms of the expectation values and the standard deviations. The expectation value of spin-Peierls domain width for every NOCI eigenstate, $\{|\Psi_k^P\rangle\}$, is defined by

$$DW_{\mathrm{sp}} = \frac{\sum_{i=1}^{25} 2(i-1)\left|\left\langle\Psi_k^P\middle|\Phi_i^P\right\rangle\right|^2}{\sum_{j=1}^{25}\left|\left\langle\Psi_k^P\middle|\Phi_j^P\right\rangle\right|^2}. \tag{33}$$

The standard deviation of the expectation value is given by

$$\sqrt{\frac{\sum_{i=1}^{25}\{2(i-1)-DW_{\mathrm{sp}}\}^2\left|\left\langle\Psi_k^P\middle|\Phi_i^P\right\rangle\right|^2}{\sum_{j=1}^{25}\left|\left\langle\Psi_k^P\middle|\Phi_j^P\right\rangle\right|^2}}. \tag{34}$$

In Fig. 5(a), the resultant expectation values and standard deviations are shown by up-triangle points and vertical bars, respectively. The corresponding eigenenergies, which are in ascending order in the diagonalized Hamiltonian $\boldsymbol{E}^P$, are shown in Fig. 5(b). As shown in Figs. 5(a) and 5(b), an eigenstate with a wider spin-Peierls domain is less stable in energy. All standard deviations of the spin-Peierls domain width are relatively small because only the NOCI bases with similar domain widths have close energies and have nonvanishing off-diagonal elements in both the Hamiltonian and the overlap matrix [Figs. S1(b) and S1(c) in the Supplemental Material [30]]. The NOCI bases with a small domain across 2 or 4 sites (i.e., $|\Phi_2^P\rangle$ and $|\Phi_3^P\rangle$) are more stable than the CDW basis $|\Phi_1^P\rangle$ due to the translation of the spin-Peierls domain incorporated in the Peierls-Yoccoz projections

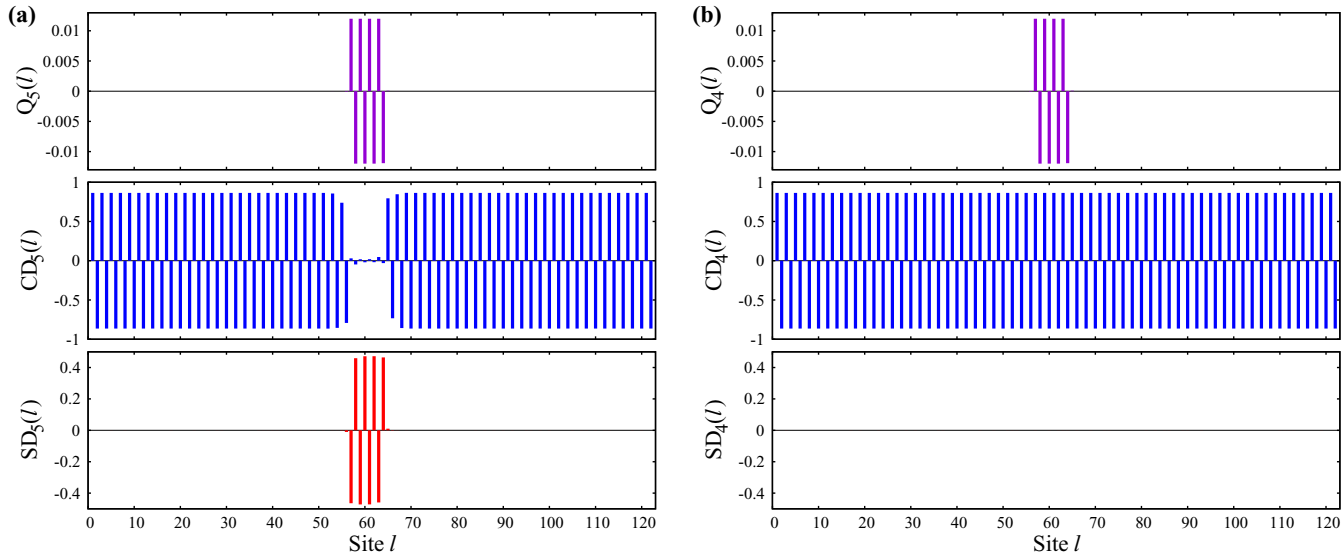

FIG. 4. Structures of the NOCI bases with a domain across eight sites: (a) spin-Peierls domain base $|\Phi_5^P\rangle$ and (b) dimerized domain base $|\Phi_4^Q\rangle$ for $N = 122$.

(Fig. S1(a) in the Supplemental Material [30]). The superposition of these bases accounts for the breathing motion of the spin-Peierls domain in the most stable NOCI eigenstate, $|\Psi_1^P\rangle$. The breathing motion in $|\Psi_1^P\rangle$ does not significantly expand the domain [$DW_{\rm sp} = 3.18$ with a standard deviation of 2.45, Fig. 5(a)] but leads to notable energy stabilization ($E_{\rm CORR} = 1.052$, Fig. 5(b)). This is consistent with the results of the ResHF calculations, as discussed above.

We next obtained the Q-space NOCI solutions ($N = 122$ and $dim(Q) = 24$) and analyzed their dimerized domain widths. Similar to Eq. (33), the expectation value of dimerized domain width for every NOCI eigenstate, $\{|\Psi_l^Q\rangle\}$, is defined by

$$DW_{\rm dim} = \frac{\sum_{i=1}^{24} 2i\left|\langle\Psi_l^Q|\Phi_i^Q\rangle\right|^2}{\sum_{j=1}^{24}\left|\langle\Psi_l^Q|\Phi_j^Q\rangle\right|^2}. \tag{35}$$

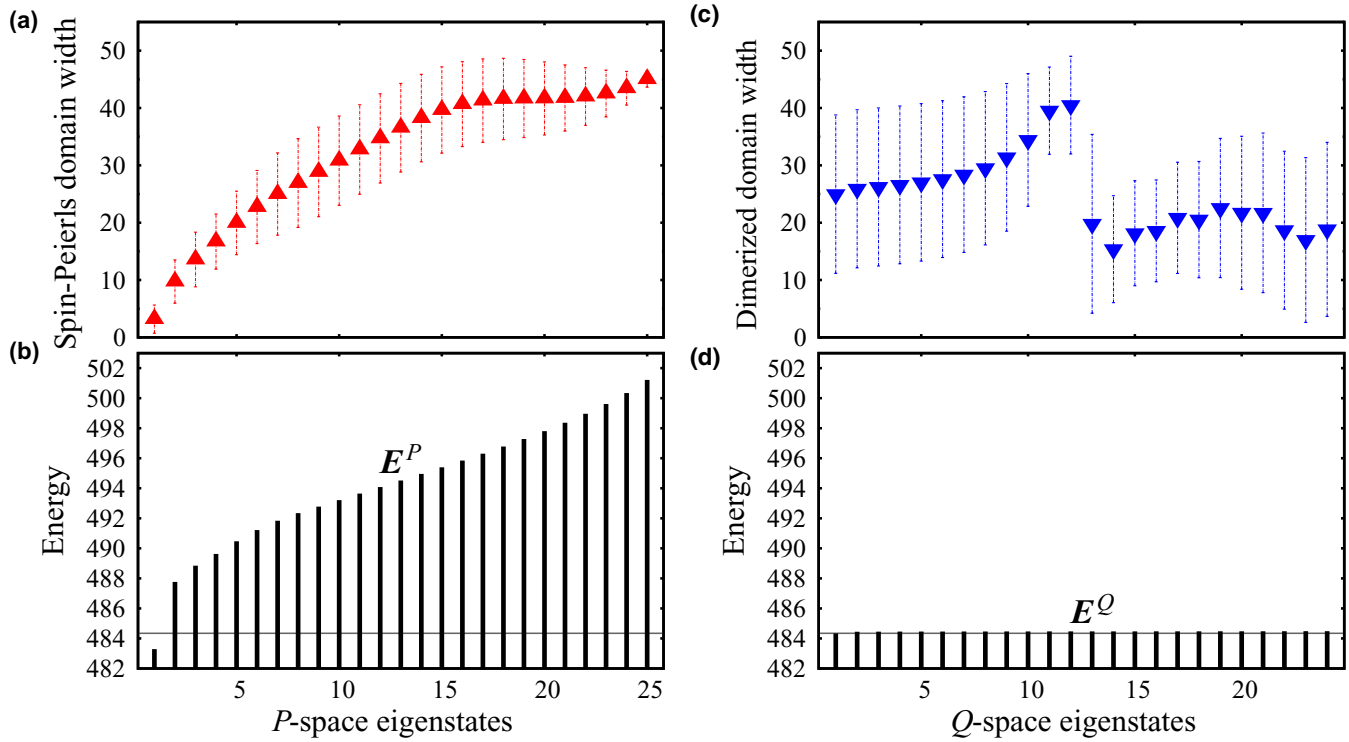

FIG. 5. Domain widths and energies of nonorthogonal configuration interaction (NOCI) eigenstates. (a) Expectation values of the spin-Peierls domain width with standard deviations (vertical bars) and (b) energies of the P-space eigenstates $\{|\Psi_k^P\rangle\}$. (c) Expectation values of the dimerized domain width with standard deviations (vertical bars) and (d) energies of the Q-space eigenstates $\{|\Psi_l^Q\rangle\}$. The horizontal baselines in panels (b) and (d) represent the energy of the CDW state $|\Phi_1^P\rangle$ ($E_{\rm CDW} = 484.342683$).

The standard deviation is given by

$$\sqrt{\frac{\sum_{i=1}^{24}(2i - DW_{\rm dim})^2 \left|\langle \Psi_l^Q | \Phi_i^Q \rangle\right|^2}{\sum_{j=1}^{24}\left|\langle \Psi_l^Q | \Phi_j^Q \rangle\right|^2}}. \tag{36}$$

The expectation values and the standard deviations are shown by down-triangle points and vertical bars, respectively, in Fig. 5(c). Most of the Q-space NOCI eigenstates, unlike the P-space ones, have wide dimerized domains, whose widths have a large standard deviation; for example, for the most stable eigenstate $|\Psi_1^Q\rangle$, $DW_{\rm dim}$ is 24.98 with a standard deviation of 13.81. This indicates the extensive superpositions of different Q-space NOCI bases $\{|\Phi_i^Q\rangle\}$, or in other words the large quantum fluctuations of the dimerized domain, such as breathing and translational motions. This is attributed to two primary reasons. Firstly, the energies of the Q-space NOCI bases are very close to $E_{\rm CDW}$ regardless of the dimerized domain widths (Fig. S2(a) in the Supplemental Material [30]). Secondly, in the Hamiltonian and the overlap matrix (Figs. S2(b) and S2(c) in the Supplemental Material [30]), the off-diagonal elements among all Q-space NOCI bases are large due to the uniform CDW electronic state and the small amplitude of dimerization distortions. Figure 5(d) shows the eigenenergies, which are in ascending order in the diagonalized Hamiltonian $\boldsymbol{E}^Q$. The energies all remain close to $E_{\rm CDW}$ [Fig. 5(d)]. Indeed, the energy of $|\Psi_1^Q\rangle$ is lower than $E_{\rm CDW}$ only by 0.009. Consequently, the breathing motion, as well as the translation, of the dimerized domain makes only a little contribution to energy stabilization; meanwhile, large breathing motions do not cause marked energy destabilization, which can facilitate the dimerized domain expansion. This contrasts with the nature of the spin-Peierls domains; recall that they cannot greatly expand but still make a major contribution to the correlation energy.

The NOCI calculation in $P+Q$ space provides an insight into the interference between the two kinds of domains with different natures. To shed light on the Q-space influence on the P-space states, for instance, it is worth studying how the P-space eigenstates are further superposed by expanding the Hilbert space to the larger $P+Q$ space. By using the NOCI eigenstates in P space and those in Q space, $P+Q$ space is spanned by

$$\left|\Psi_1^P\right\rangle, \left|\Psi_2^P\right\rangle, \cdots, \left|\Psi_{dim(P)}^P\right\rangle, \left|\Psi_1^Q\right\rangle, \left|\Psi_2^Q\right\rangle, \cdots, \left|\Psi_{dim(Q)}^Q\right\rangle. \tag{37}$$

We focus on the ground state, whose NOCI wave function is written as

$$|\Psi_{\rm gs}\rangle = \sum_{k=1}^{dim(P)} D_k^P \left|\Psi_k^P\right\rangle + \sum_{l=1}^{dim(Q)} D_l^Q \left|\Psi_l^Q\right\rangle. \tag{38}$$

The expansion coefficients and the energy are determined by

$$\begin{pmatrix} \boldsymbol{E}^P & \boldsymbol{H}^{PQ} \\ \boldsymbol{H}^{QP} & \boldsymbol{E}^Q \end{pmatrix} \begin{pmatrix} \boldsymbol{D}^P \\ \boldsymbol{D}^Q \end{pmatrix} = E_{\rm gs} \begin{pmatrix} \boldsymbol{I} & \boldsymbol{S}^{PQ} \\ \boldsymbol{S}^{QP} & \boldsymbol{I} \end{pmatrix} \begin{pmatrix} \boldsymbol{D}^P \\ \boldsymbol{D}^Q \end{pmatrix}, \tag{39}$$

where the Hamiltonian and the overlap matrix have nonzero PQ and QP blocks since P and Q spaces are mutually nonorthogonal. $\boldsymbol{E}^P$ and $\boldsymbol{E}^Q$ are the diagonal Hamiltonian matrices whose entries are in ascending order [Figs. 5(b) and 5(d)]. Instead of directly solving this NOCI equation, we here choose an equivalent but different approach, that is, Löwdin-Feshbach partitioning method [24–29]. When applying this method, we shall select P space as the model space of interest and Q space as the external space to clarify the influence of Q space on P space. An eigenvalue equation for the model P space is then derived as follows:

$$\boldsymbol{H}_{\rm eff}\boldsymbol{D}^P = E_{\rm gs}\boldsymbol{D}^P. \tag{40}$$

This indicates that when an effective Hamiltonian $\boldsymbol{H}_{\rm eff}$ operates on its eigenstate $\boldsymbol{D}^P$, the projection of the ground state onto the model space, it yields the ground-state energy in Eq. (39). Such an effective Hamiltonian is given by

$$\boldsymbol{H}_{\rm eff} = \boldsymbol{E}^P + (\boldsymbol{H}^{PQ} - E_{\rm gs}\boldsymbol{S}^{PQ}) \times (E_{\rm gs}\boldsymbol{I} - \boldsymbol{E}^Q)^{-1}(\boldsymbol{H}^{QP} - E_{\rm gs}\boldsymbol{S}^{QP}). \tag{41}$$

The second term in Eq. (41), or $\boldsymbol{H}_{\rm eff} - \boldsymbol{E}^P$, represents the influence of the external Q space on the model P space. Note that $\boldsymbol{E}^P$ is already diagonal, and $\boldsymbol{H}_{\rm eff} - \boldsymbol{E}^P$ is zero if there is no Q-space influence. Hence, we will discuss the matrix structure of $\boldsymbol{H}_{\rm eff} - \boldsymbol{E}^P$ to understand how the spin-Peierls domain states $\{|\Psi_k^P\rangle\}$ are stabilized and/or mutually superposed under the influence of the dimerized domain states $\{|\Psi_l^Q\rangle\}$.

The diagonal elements and the contour map of $\boldsymbol{H}_{\rm eff} - \boldsymbol{E}^P$, including the off-diagonal elements, are shown in Figs. 6(a)

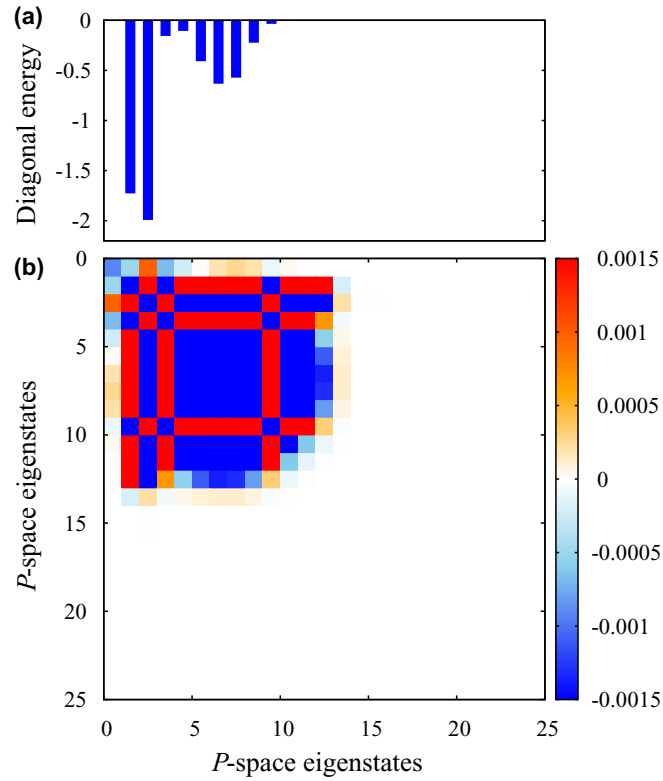

FIG. 6. Influence of the dimerized-domain Q space on the spin-Peierls-domain P space. (a) Diagonal energies and (b) the contour map of $\boldsymbol{H}_{\rm eff} - \boldsymbol{E}^P$ in its matrix representation in the P-space eigenstate bases, $\{|\Psi_k^P\rangle\}$.

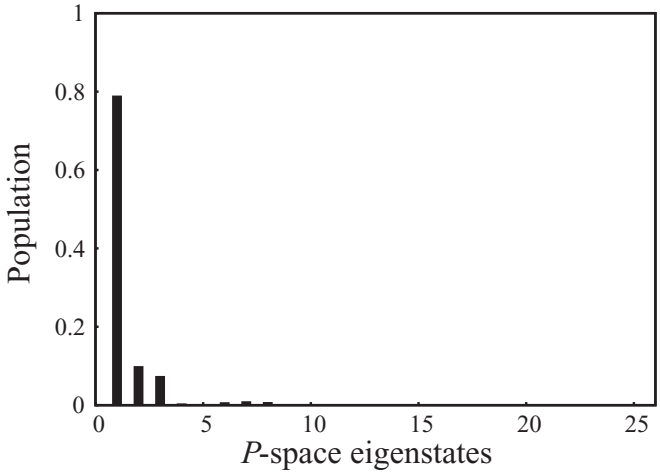

FIG. 7. Population $|D_k^P|^2$ of each spin-Peierls-domain state $|\Psi_k^P\rangle$ in the ground state, obtained by diagonalizing $\boldsymbol{H}_{\rm eff}$.

and 6(b). Since $E_l^Q \approx E_{\rm CDW}$ for $l = 1, 2, \ldots, dim(Q)$, as is discussed in Fig. 5(d),

$$\boldsymbol{H}_{\rm eff} - \boldsymbol{E}^P \approx \frac{(\boldsymbol{H}^{PQ} - E_{\rm gs}\boldsymbol{S}^{PQ})(\boldsymbol{H}^{QP} - E_{\rm gs}\boldsymbol{S}^{QP})}{E_{\rm gs} - E_{\rm CDW}}. \quad (42)$$

The matrix structure in Fig. 6(b) is thus primarily determined by the PQ and QP blocks of the Hamiltonian and the overlap matrix in Eq. (39). In these blocks, Hamiltonian and overlap matrix elements are nonvanishing between small spin-Peierls domain states and most of the dimerized domain states with various domain widths (Figs. S3(a) and S3(b) in the Supplemental Material [30]). Therefore, the upper-left area in Fig. 6(b), corresponding to the block of small spin-Peierls domains, has nonzero $\boldsymbol{H}_{\rm eff} - \boldsymbol{E}^P$ elements due to the strong influence of the dimerized-domain Q space. In Fig. 6(a), the negligibly small diagonal (1, 1) element of $\boldsymbol{H}_{\rm eff} - \boldsymbol{E}^P$ indicates that $|\Psi_1^P\rangle$, the most stable eigenstate in P space, is not further stabilized by the diagonal component. In contrast, the large negative values of the (2, 2) and (3, 3) elements of $\boldsymbol{H}_{\rm eff} - \boldsymbol{E}^P$ indicate that $|\Psi_2^P\rangle$ and $|\Psi_3^P\rangle$ states with slightly different spin-Peierls domain widths [Fig. 5(a)] are particularly stabilized due to the influence of the dimerized domain states. In addition, $|\Psi_1^P\rangle$, $|\Psi_2^P\rangle$, and $|\Psi_3^P\rangle$ states mutually interact through the off-diagonal $\boldsymbol{H}_{\rm eff} - \boldsymbol{E}^P$ elements. These Q-space influences on both diagonal and off-diagonal elements lead to the superposition among the three P-space states in the ground state (Fig. 7), which is obtained after the diagonalization of $\boldsymbol{H}_{\rm eff}$. Note that this Q-space-induced superposition has only a minor effect on the correlation energy (i.e., 0.002). To sum up, the existence of the dimerized domain states affects the superposition between the regular CDW state and various spin-Peierls domain states, which can be critical when interpreting the electric-field responses as will be explained below.

In the thermodynamic limit, the spin-Peierls domain width would slightly increase but is unlikely to diverge to infinity [Fig. 8(a)]. This suggests that the density of the spin-Peierls domain remains zero even when considering the quantum fluctuations discussed above. Nevertheless, the quantum

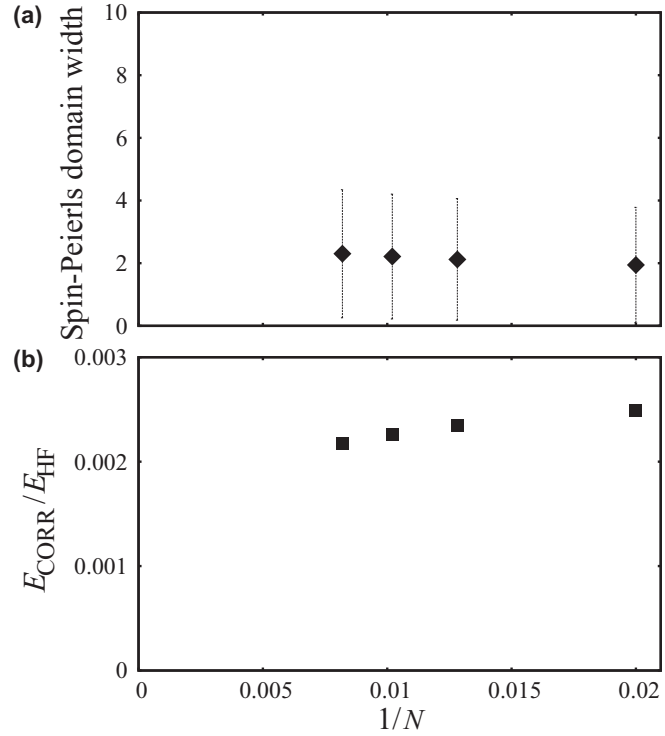

FIG. 8. System-size dependence ($N = 50, 78, 98, 122$) on the ground-state properties: (a) expectation values (diamond points) and standard deviations (vertical bars) of the spin-Peierls domain width and (b) energy ratio of $E_{\rm CORR}/E_{\rm HF}$. $dim(P)$ and $dim(Q)$ are 25 and 24, respectively.

fluctuations affect the correlation energy. $E_{\rm CORR}/E_{\rm HF}$ is very likely to have a nonzero finite value in the thermodynamic limit [Fig. 8(b)]. All of these NOCI results are consistent with the ResHF results (see Fig. 3 for the ResHF correlation energy).

C. Insights into the fast charge and lattice responses of TTF-CA to femtosecond electric-field pulses

We focus on two recent pump-probe studies on the neutral phase of TTF-CA [23,42]. One of them reported a photoinduced neutral-ionic (NI) transition by using 15-fs laser pulses [42], and the other revealed that a THz pump pulse produces a large macroscopic polarization partly due to the ionic domain expansion and shrinking [23]. In both experiments, the observed transient reflectivity, a good probe of charge transfer, is explained by the displacive excitation of coherent phonons (DECP) mechanism [43]. The mechanism comprises the following sequential processes: (i) instant intermolecular electron transfer and (ii) subsequent decays involving coherent vibrational motions. For the first process, the NI transition study suggests that the 15-fs pump pulse would generate ionic domains in 20 fs without spin-Peierls dimerization [42]. The THz pump-probe study also suggests an initial electronic response without lattice motions [23]. In contrast, we found the electron-lattice states with dimerized ionic (spin-Peierls) and neutral (CDW) domains in the ground-state ResHF wave

function, which is schematically shown by

$$
\begin{aligned}
|\Psi\rangle = {} & C_1|\cdots \mathrm{D}^0\mathrm{A}^0\mathrm{D}^0\mathrm{A}^0\cdots\rangle \\
& + C_2|\cdots \mathrm{D}^0\mathrm{A}^0\,\underline{\mathrm{D}^+\mathrm{A}^-}\,\underline{\mathrm{D}^+\mathrm{A}^-}\,\mathrm{D}^0\mathrm{A}^0\cdots\rangle \\
& + C_3|\cdots \mathrm{D}^0\mathrm{A}^0\,\underline{\mathrm{D}^+\mathrm{A}^-}\,\underline{\mathrm{D}^+\mathrm{A}^-}\,\underline{\mathrm{D}^+\mathrm{A}^-}\,\mathrm{D}^0\mathrm{A}^0\cdots\rangle \\
& + C_4|\cdots \mathrm{D}^0\mathrm{A}^0\,\underline{\mathrm{D}^0\mathrm{A}^0}\,\underline{\mathrm{D}^0\mathrm{A}^0}\,\mathrm{D}^0\mathrm{A}^0\cdots\rangle \\
& + C_5|\cdots \mathrm{D}^0\mathrm{A}^0\,\underline{\mathrm{D}^0\mathrm{A}^0}\,\underline{\mathrm{D}^0\mathrm{A}^0}\,\underline{\mathrm{D}^0\mathrm{A}^0}\,\mathrm{D}^0\mathrm{A}^0\cdots\rangle + \cdots .
\end{aligned}
\tag{43}
$$

The underlines shown above represent the lattice dimerization. Supposing that the weight of each electron-lattice state in Eq. (43) is instantly changed by the pump pulse, the expectation value of the dimerized ionic domain width can accordingly change. For example, Franck-Condon excitation of dimerized neutral domains will generate dimerized ionic domains (i.e., increased populations of $|C_2|^2$ and $|C_3|^2$ and decreased populations of $|C_4|^2$ and $|C_5|^2$). These suggest that not only the equidistant ionic domains but also the dimerized ionic domains can be immediately generated by a femtosecond pulse.

We next discuss the subsequent process involving coherent vibrational motions. Both experiments attribute the coherent oscillation with a frequency of 54 cm^{-1} to the spin-Peierls dimerization in the generated ionic domains [23,42]. The THz pump-probe study further clarified that the ionic domain expansion/shrinking, or breathing oscillations of NI domain walls, is slowed down by the accompanying lattice dimerization [23]. These indicate that the ionic domains in the neutral phase are stabilized by the spin-Peierls mechanism, which is consistent with the spin-Peierls domains found in the ResHF solutions. The NOCI calculations revealed that the spin-Peierls domain bases directly interact through the off-diagonal P-space Hamiltonian/overlap elements. The spin-Peierls domain bases also show the indirect interference via the dimerized CDW domain bases, as is seen in the nondiagonal effective Hamiltonian. These direct and indirect interferences between different spin-Peierls domain bases can facilitate the NI domain wall motions under a THz electric field.

V. SUMMARY

By applying the nonadiabatic ResHF theory to the extended Hubbard model incorporating a staggered site-diagonal potential and the SSH electron-phonon coupling, we clarified the quantum fluctuations in the correlated CDW ground state of TTF-CA. We found two kinds of distinctive domain structures: ionic domains with spin-Peierls dimerization and neutral dimerized domains in the regular CDW phase. The domain walls connecting the neutral and ionic states have already been believed to be important especially near the phase boundary. However, this picture is usually discussed on the basis of the HF approximation or simplified noninteracting models. The present research, based on the ResHF wave functions, clarified that the ionic (or spin-Peierls) domains inherently exist in the neutral (CDW) ground state as quantum fluctuations even in the parameter regime rather far from the phase boundary. We should also note that the spin-Peierls domain has a dimerized lattice. Furthermore, the dimerized CDW domain is a new concept, as the CDW state is believed to exist on the equidistant lattice. The most important point is such intuitive pictures are obtained by the many-body theory beyond the adiabatic approximation. The spin-Peierls domains do not easily expand in the ground state (i.e., zero domain density in the thermodynamic limit) but still notably contribute to the correlation energy. By contrast, the dimerized CDW domains can greatly expand, which has little effect on the correlation energy. The configuration interaction calculations and the Löwdin-Feshbach partitioning indicate that spin-Peierls domain states with different domain widths can directly and indirectly interact. The indirect interference is mediated by the dimerized domain states. Beyond the conventional picture of the fast charge and lattice responses of TTF-CA to femtosecond pulses, our intuitive visualization of the ground-state wave function demonstrates the importance of the quantum fluctuations. An in-depth dynamics study on the roles of the quantum fluctuations (e.g., the dimerized CDW domains as precursors facilitating the spin-Peierls domain growth) will serve as a firm basis for the experimental ultrafast control of polarization of the organic CT family.

[1] T. Misawa, S. Morita, K. Yoshimi, M. Kawamura, Y. Motoyama, K. Ido, T. Ohgoe, M. Imada, and T. Kato, Comput. Phys. Commun. **235**, 447 (2019).
[2] E. Jeckelmann and S. R. White, Phys. Rev. B **57**, 6376 (1998).
[3] H. Matsueda, T. Tohyama, and S. Maekawa, Phys. Rev. B **74**, 241103(R) (2006).
[4] W. P. Su, J. R. Schrieffer, and A. J. Heeger, Phys. Rev. Lett. **42**, 1698 (1979).
[5] K. Shida, Y. Watanabe, H. Gomi, A. Takahashi, and N. Tomita, J. Phys. Soc. Jpn. **84**, 124803 (2015).
[6] N. Tomita and A. Takahashi, Phys. Rev. B **99**, 035203 (2019).
[7] N. Nagaosa and J. Takimoto, J. Phys. Soc. Jpn. **55**, 2735 (1986).
[8] N. Nagaosa and J. Takimoto, J. Phys. Soc. Jpn. **55**, 2745 (1986).
[9] T. Iizuka-Sasano and Y. Toyozawa, J. Phys. Soc. Jpn. **65**, 671 (1995).
[10] P. Huai, H. Zheng, and K. Nasu, J. Phys. Soc. Jpn. **69**, 1788 (2000).
[11] N. Miyashita, M. Kuwabara, and K. Yonemitsu, J. Phys. Soc. Jpn. **72**, 2282 (2003).
[12] K. Yonemitsu, J. Phys. Soc. Jpn. **73**, 2868 (2004).
[13] K. Iwano, Phys. Rev. Lett. **97**, 226404 (2006).
[14] N. Nagaosa, J. Phys. Soc. Jpn. **55**, 2754 (1986).
[15] L. DelFreo, A. Painelli, and Z. G. Soos, Phys. Rev. Lett. **89**, 027402 (2002).
[16] G. Giovannetti, S. Kumar, A. Stroppa, J. van den Brink, and S. Picozzi, Phys. Rev. Lett. **103**, 266401 (2009).
[17] M. Tsuchiizu, H. Yoshioka, and H. Seo, J. Phys. Soc. Jpn. **85**, 104705 (2016).
[18] J. B. Torrance, A. Girlando, J. J. Mayerle, J. I. Crowley, V. Y. Lee, P. Batail, and S. J. LaPlaca, Phys. Rev. Lett. **47**, 1747 (1981).

[19] M. Le Cointe, M. H. Lemee-Cailleau, H. Cailleau, B. Toudic, L. Toupet, G. Heger, F. Moussa, P. Schweiss, K. H. Kraft, and N. Karl, Phys. Rev. B **51**, 3374 (1995).
[20] S. Horiuchi, Y. Okimoto, R. Kumai, and Y. Tokura, J. Phys. Soc. Jpn. **69**, 1302 (2000).
[21] K. Kobayashi, S. Horiuchi, R. Kumai, F. Kagawa, Y. Murakami, and Y. Tokura, Phys. Rev. Lett. **108**, 237601 (2012).
[22] T. Miyamoto, H. Yada, H. Yamakawa, and H. Okamoto, Nat. Commun. **4**, 2586 (2013).
[23] T. Morimoto, T. Miyamoto, H. Yamakawa, T. Terashige, T. Ono, N. Kida, and H. Okamoto, Phys. Rev. Lett. **118**, 107602 (2017).
[24] H. Feshbach, Ann. Phys. (NY) **5**, 357 (1958).
[25] H. Feshbach, Ann. Phys. (NY) **19**, 287 (1962).
[26] P. O. Löwdin, J. Math. Phys. **3**, 969 (1962).
[27] P. O. Löwdin, J. Mol. Spectrosc. **10**, 12 (1963).
[28] P. O. Löwdin, J. Mol. Spectrosc. **14**, 112 (1964).
[29] P. O. Löwdin, J. Chem. Phys. **11**, 1396 (1951).
[30] See Supplemental Material at http://link.aps.org/supplemental/10.1103/PhysRevB.100.205205 for the scaling procedure for deriving Eq. (1), and Hamiltonian and overlap matrices in their representation in the P-space bases $\{|\Phi_i^P\rangle\}$, the Q-space bases $\{|\Phi_i^Q\rangle\}$, and the $P+Q$-space bases in Eq. (37).
[31] G. D'Avino, A. Girlando, A. Painelli, M. H. Lemee-Cailleau, and Z. G. Soos, Phys. Rev. Lett. **99**, 156407 (2007).
[32] H. Takayama, Y. R. Lin-Liu, and K. Maki, Phys. Rev. B **21**, 2388 (1980).
[33] C. Katan, C. Koenig, and P. E. Bröchl, Solid State Commun. **102**, 589 (1997).
[34] G. D'Avino and M. J. Verstraete, Phys. Rev. Lett. **113**, 237602 (2014).
[35] R. E. Peierls and J. Yoccoz, Proc. Phys. Soc., London, Sect. A **70**, 381 (1957).
[36] Y. G. Smeyers and L. Doreste-Suarez, Int. J. Quantum Chem. **52**, 687 (1973).
[37] A. Igawa, Int. J. Quantum Chem. **54**, 235 (1995).
[38] A. Ikawa, S. Yamamoto, and H. Fukutome, J. Phys. Soc. Jpn. **62**, 1653 (1993).
[39] N. Tomita, S. Ten-no, and Y. Tanimura, Chem. Phys. Lett. **263**, 687 (1996).
[40] N. Tomita, Phys. Rev. B **69**, 045110 (2004).
[41] H. Fukutome, Prog. Theor. Phys. **80**, 417 (1988).
[42] H. Uemura and H. Okamoto, Phys. Rev. Lett. **105**, 258302 (2010).
[43] H. J. Zeiger, J. Vidal, T. K. Cheng, E. P. Ippen, G. Dresselhaus, and M. S. Dresselhaus, Phys. Rev. B **45**, 768 (1992).